



Modeling and testing of a field-controllable magnetorheological fluid damper

Şevki Çeşmeci, Tahsin Engin*

University of Sakarya, Department of Mechanical Engineering, Esentepe Campus, 54187 Sakarya, Turkey

ARTICLE INFO

Article history:

Received 6 February 2009

Received in revised form

16 April 2010

Accepted 26 April 2010

Available online 4 May 2010

Keywords:

Semi-active vibration control

Magnetorheological damper

MR/ER damper

MR fluids

Bingham plastic flow model

Modified Bouc–Wen model

ABSTRACT

In this study, an experimental and a theoretical study were carried out to predict the dynamic performance of a linear magnetorheological (MR) fluid damper. After having designed and fabricated the MR damper, its dynamic testing was performed on a mechanical type shock machine under sinusoidal excitation. A theoretical flow analysis was done based on the Bingham plastic constitutive model to predict the behavior of the prototyped MR damper. The theoretical results were then validated by comparing them against experimental data, and it was shown that the flow model can accurately capture the dynamic force range of the MR damper. In addition to the flow model, a modified parametric algebraic model was proposed to capture the hysteretic behavior of the MR damper. The superiority of the proposed modified model was shown by comparing it with the Alg model as well as with a widely adopted modified Bouc–Wen model through an error analysis. It is observed that although all the three models are comparable at the excitation velocities of 0.05, 0.10, and 0.15 m/s, the mAlg model is remarkably successful at the highest excitation velocity of 0.2 m/s over the other two. The improvements in the predictions were found to be over 50%, relative to unmodified model especially at lower current inputs. Therefore, it was concluded that the present flow model can be successfully adopted to design and predict the dynamic behavior of MR dampers, while the mAlg model can be used to develop more effective control algorithms for such devices.

© 2010 Elsevier Ltd. All rights reserved.

1. Introduction

Magnetorheological (MR) fluids are suspensions of soft particles, having a diameter of 1–5 μm , in a special carrier liquid such as water, mineral oil, synthetic oil, and glycol. The essential feature of the MR fluids is that they can reversibly change their states from a Newtonian fluid to a semi-solid or even a solid with controllable dynamic yield stress within a few milliseconds, when they are subjected to a controlled magnetic field [1]. Over the past decade, there has been an increasing interest in the MR fluids and their engineering applications. This is likely due to the controllable interface produced by the MR fluid enabling the device to interact with a controller to continuously regulate the mechanical output the device. MR dampers are one of the most promising new semi-active devices for semi-active control of mechanical vibration. These dampers have attracted very much interest of suspension designers and researchers due to their variable damping feature, mechanical simplicity, robustness, low power consumption, and fast response. MR dampers are not only advantageous in their ability to provide variable damping forces to the suspension; they are also inherently fail-safe devices from an electronic point of view [2]. If there was a fault in the system, the MR damper could act as a passive damping device within

certain performance parameters. Potential applications of MR dampers include the areas of automotive and aerospace industries [3,4,5], seismic protection of bridges and buildings [6,7].

MR fluids demonstrate highly nonlinear complex behavior due to the applied magnetic field, applied load, strain amplitude and frequency of excitation in the dynamic conditions. A great effort has been made to characterize the nonlinear properties of MR devices in the literature. However, accurate models are still needed in order to understand and predict the operational and dynamic behavior of such devices. Although various models both in non-parametric and parametric have been recently proposed to capture the dynamic behavior of MR fluids and their devices, the simplest one is the Bingham plastic model, which is a steady-state model assuming that the fluid is in the post-yield phase and is flowing at a constant shear rate [2,8,9,10]. However, since the magnetically active gap, through which MR fluid flows, is relatively small compared to radius of annulus, it is seen in the literature that the infinitely wide parallel-plate approximation of the flow has been extensively used to capture the dynamic behavior of MR dampers [11,12].

In the present study, a theoretical flow analysis was made in order to predict the behavior of a field-controllable magnetorheological fluid damper. The flow analysis uses simple Bingham plastic constitutive model for the dynamic shear stress in order to account for non-Newtonian characteristic of the MR fluid. The theoretical results were then validated by comparing them against the experimental data. To do this, an MR damper was designed, fabricated, and tested at the Applied Fluid Mechanics Laboratory

* Corresponding author. Tel.: +90 264 295 5859; fax: +90 264 295 5601.

E-mail addresses: scesmeci@sakarya.edu.tr (Ş. Çeşmeci), engin@sakarya.edu.tr (T. Engin).

Symbols

a	Inner plug radius measured from shaft axis, displacement amplitude
A_p	Frontal area of the piston head
A_s	Cross-sectional area of the shaft
b	Outer plug radius measured from shaft axis
C	Integral constant
D	Dynamic range
$D_{\text{channel},i}$	Inner diameter of the flow channel
$D_{\text{channel},o}$	Outer diameter of the flow channel
$D_{\text{cyl},i}$	Inner diameter of the cylinder
D_p	Diameter of the piston head
D_s	Shaft diameter
F	Damping force
$F_{\text{compression}}$	Damping force of the MR damper when it is in compression mode
F_{exp}	Measured force
F_f	Friction force
F_{gas}	Gas force
F_{pre}	Predicted force
F_{rebound}	Damping force of the MR damper when it is in rebound mode
g	Gap of the flow channel
H	Applied magnetic field intensity
I	Current
K	Fluid index
L	Length of the flow channel
L_{active}	Active pole length
L_{damper}	Total length of the damper at its maximum extension
L_{inactive}	Inactive pole length
n	Fluid index
P	Pressure
Q	Volume flow rate
Q_p	Volume flow rate displaced by the piston head

Q_T	Total volume flow rate through the flow channel
r	Radial coordinate measured from the shaft axis
R_1	Inner radius of the flow channel measured from the shaft axis
R_2	Outer radius of the flow channel measured from the shaft axis
S	Maximum stroke
$u(r)$	Velocity distribution in the flow channel
V_p	Piston velocity
w	Width of the flow channel
x	Longitudinal coordinate
$\dot{\gamma}$	Shear-strain rate
ΔP_μ	Viscous component of the pressure drop
ΔP_τ	Field-dependent induced yield stress component of the pressure drop
μ	Plastic viscosity
τ	Shear stress
μ_F	Mean measured force
τ_y	Dynamic yield stress
ΔP	Pressure drop across annular gap
ω	Angular velocity

Brevities

Alg	Algebraic model
$mAlg$	Modified algebraic model
mBW	Modified Bouc-Wen model

Subscripts

Alg	Algebraic model
$mAlg$	Modified algebraic model
t	Time
x	Displacement
\dot{x}	Velocity

(AFML), University of Sakarya. It was shown that the developed model can accurately capture the nonlinear behavior of the MR damper, and can be used to analyze, design and develop control algorithms for MR dampers. One major deficiency associated with the present flow modeling is the fact that it cannot characterize the hysteretic behavior of the MR damper, which is the case when hysteretic loop is relatively large. This is crucially important so as to electronically control the vibration of a mechanical system equipped with MR dampers. For this reason, a parametric mechanical model [1] was adopted and modified to improve its capability of capturing the hysteretic loop of the MR damper, and the associated parameters were determined by the least-square method.

2. Magnetorheological fluid damper configuration

Most devices that use MR fluids can be classified as having either fixed poles (pressure driven flow mode) or relatively

moveable poles (direct-shear mode). Schematic for the two basic operational modes are given in Fig. 1.

The hydraulic devices that use MR fluids, including dampers, servo-valves, shock absorbers, are generally in pressure driven flow mode while MR brakes and clutches are in direct-shear mode. A schematic diagram for the damper used in this study is given in Fig. 2 with its primary components. The portions denoted as A and B in Fig. 2 are filled with MR fluids whereas the accumulator, which is for compensating the additional volume into the chamber caused by the movement of the piston rod, is filled with the pressurized nitrogen gas. The MR fluid used in this study is MRF-122ED of Lord Corporation. During the motion of the MR damper's piston rod, fluid flows through the annular gap opened on the piston head. Inside the piston head, a coil is wound around the bobbin shaft with an insulated wire. When electrical current is applied to the coil, a magnetic field develops around the piston head. The magnetic flux lines will look like as shown in Fig. 2.

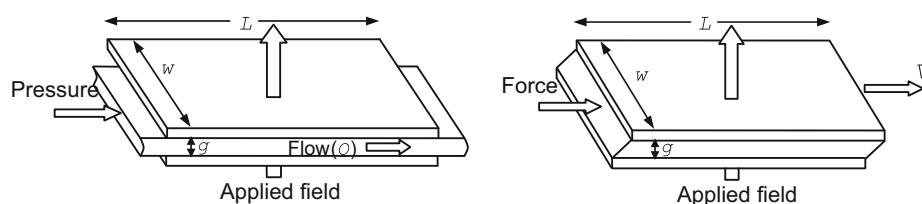


Fig. 1. Basic operational modes for field-controllable fluid devices: (a) pressure driven flow mode and (b) direct-shear mode.

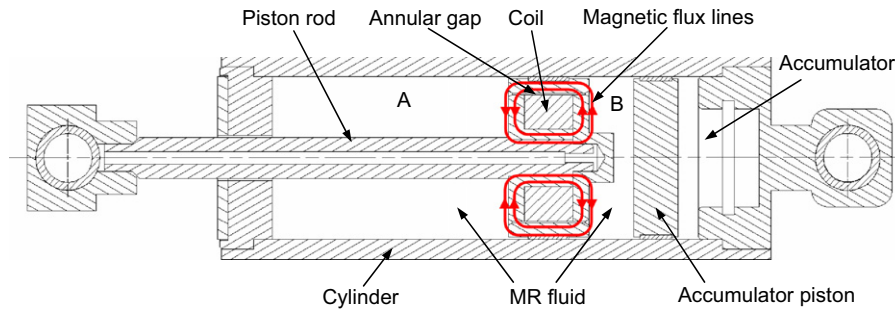


Fig. 2. Cross-sectional view of the prototyped damper, SAUMRD002.

All components of the MR damper are made from stainless steel. However, the piston head is made from austenitic stainless steel due to its poor magnetic properties to minimize the loss of magnetic flux. Special PTFE-based bearing materials are used to minimize the friction forces in the piston head, shaft bearing and accumulator piston. A wiper-type dynamic shaft seal is used to ensure the fluid is constrained inside the cylinder.

The magnetically induced iron particles inside the MR fluid arrays in the direction of the magnetic flux lines to resist the flow, thus generating a damping force. The mechanical energy required to yield this chain-like structure increases as the applied field increases resulting in a field-dependent yield stress. Therefore, the behavior of MR fluid is often represented as Bingham plastic having a variable yield stress. The Bingham plastic model is given by

$$\tau = \tau_y(H)\text{sgn}\left(\frac{du}{dr}\right) + \mu \frac{du}{dr} \quad |\tau| > |\tau_y| \quad (1)$$

$$\frac{du}{dr} = 0 \quad |\tau| < |\tau_y| \quad (2)$$

where τ is the shear stress, τ_y is the dynamic yield stress, H is the applied magnetic field intensity, du/dr is the shear-strain rate, and μ is the plastic viscosity of the MR fluid. However, true MR fluid behavior exhibits some departures from Bingham plastic model. One and may be the most significant of these departures involves the non-Newtonian behavior of the MR fluid in the presence of an applied field. Still, if used properly, Eqs. (1) and (2) work well for the preliminary design of MR dampers as well as other MR fluid devices. Additional design considerations are available in the literature such as [2].

3. Quasi-static analysis of flow in the MR damper

Several methods have been proposed in the literature to model the flow inside an MR damper. In this section, the quasi-static axisymmetric model, which was firstly suggested by Gavin et al. [13] and later successfully used by Yang et al. [14] in their study where they compared the model with both a simple parallel-plate model and experimental results, is utilized. The quasi-static analysis is based on the following assumptions: (1) MR damper moves at a constant velocity, (2) the flow is fully developed in the annular gap, and (3) a simple Bingham plastic model can be applied to describe the MR fluid behavior.

The Bingham plastic model considers a dynamic yield stress, below which the fluid acts like a rigid body. This region is referred as plug region. In the plug region (also called as core or pre-yield region), the local shear stresses have not yet exceeded the dynamic yield stress thus the fluid does not shear, but moves like a solid body. When the local shear stresses exceed the dynamic yield stress, then the fluid acts like a viscous fluid. These

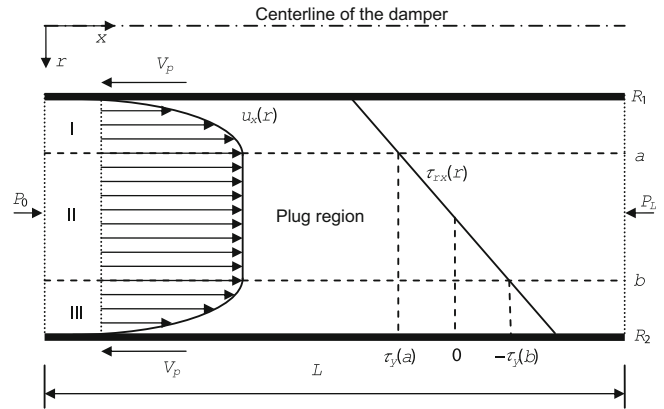


Fig. 3. Stress and velocity profiles across annular duct.

regions are called as post-yield region. The pre- and post-yield regions are shown in Fig. 3 with the stress and velocity profiles. As shown in Fig. 3, the velocity profile is divided into three regions: Region I, II and III. Region I and III denote the post-yield regions, whereas region II denotes the pre-yield region.

Following additional assumptions are made to model the flow through the annulus properly: (1) The flow is steady and incompressible, (2) the flow is fully developed and laminar, (3) the velocity field is axisymmetric with no swirl, implying that $u_\theta=0$ and all partial derivatives with respect to θ are zero, (4) a constant pressure gradient, dP/dx is applied in the x -direction such that pressure changes linearly with respect to x , (5) gravitational effects are ignored, and (6) the flow is only in the x -direction; implying that $u_r=0$ and all partial derivatives with respect to r are zero. Simplifying the continuity and the Navier–Stokes equations in cylindrical coordinates with respect to the above assumptions yields

$$\frac{1}{\mu} \frac{\partial P}{\partial x} = \frac{1}{r} \frac{\partial}{\partial r} \left(r \frac{\partial u_x}{\partial r} \right) \quad (3)$$

Recalling that $\tau_{rx} = -\mu \frac{\partial u_x}{\partial r}$ in laminar flow, Eq. (3) can be rearranged as

$$\frac{d(\tau_{rx} \cdot r)}{dr} = \frac{dP}{dx} r \quad (4)$$

The assumption of steady flow may be questionable if the flow is high-frequency oscillatory or unsteady. In such a case, inertial terms in the Navier–Stokes equations should be taken into account conveniently. Integrating Eq. (4) once with respect to r and solving for τ_{rx} gives

$$\tau_{rx} = \frac{1}{2} \frac{dP}{dx} r + \frac{C_1}{r} \quad (5)$$

Bingham plastic model describes the yield stress as in Eqs. (1) and (2). Because of their different natures, each region in Fig. 3 should be evaluated separately. In region I, the shear stress is given by

$$\tau_{rx}(r) = \tau_y + \mu \frac{du(r)}{dr} \quad (du/dr > 0, \text{ and thus } \text{sgn}(du/dr) = 1) \quad (6)$$

Substituting Eq. (6) into Eq. (5) gives

$$\tau_y + \mu \frac{du(r)}{dr} = \frac{1}{2} \frac{dP}{dx} r + \frac{C_1}{r} \quad (7)$$

rearranging

$$\frac{du(r)}{dr} = \frac{1}{2\mu} \frac{dP}{dx} r + \frac{C_1}{\mu r} - \frac{\tau_y}{\mu} \quad (8)$$

integrating once with respect to r

$$u(r) = \frac{1}{4\mu} \frac{dP}{dx} r^2 + \frac{C_1}{\mu} \ln(r) - \frac{\tau_y}{\mu} r + C_2 \quad (9)$$

where C_1 and C_2 are the integral constants which can be determined by the boundary conditions in region I. Boundary conditions for each region are listed in Table 1.

One can conclude with

$$u(r) = -\frac{1}{4\mu} \frac{dP}{dx} (R_1^2 - r^2) + \frac{C_1}{\mu} \ln\left(\frac{r}{R_1}\right) - \frac{\tau_y}{\mu} (r - R_1) - V_p; \quad R_1 \leq r \leq a \quad (10)$$

by applying the boundary condition given for region I. In region III, the shear stress is given by

$$\tau_{rx}(r) = -\tau_y + \mu \frac{du(r)}{dr} \quad (du/dr < 0, \text{ and thus } \text{sgn}(du/dr) = -1) \quad (11)$$

In a similar fashion as we did for region I, one can end up with

$$u(r) = -\frac{1}{4\mu} \frac{dP}{dx} (R_2^2 - r^2) + \frac{C_1}{\mu} \ln\left(\frac{r}{R_2}\right) - \frac{\tau_y}{\mu} (R_2 - r) - V_p; \quad b \leq r \leq R_2 \quad (12)$$

for region III. It is evident from Fig. 3 that $du(r)/dr = 0$ across the plug region, thus $u(r=a)$ must be equal to $u(r=b)$, which yields

$$\begin{aligned} & -\frac{1}{4\mu} \frac{dP}{dx} (R_1^2 - a^2) + \frac{C_1}{\mu} \ln\left(\frac{a}{R_1}\right) - \frac{\tau_y}{\mu} (a - R_1) - V_p \\ & = -\frac{1}{4\mu} \frac{dP}{dx} (R_2^2 - r^2) + \frac{C_1}{\mu} \ln\left(\frac{r}{R_2}\right) - \frac{\tau_y}{\mu} (R_2 - r) - V_p \end{aligned} \quad (13)$$

or

$$\frac{dP}{dx} = \frac{4}{R_1^2 - R_2^2 + b^2 - a^2} \left[D_1 \ln\left(\frac{a R_2}{b R_1}\right) + \tau_y (R_1 + R_2 - a - b) \right] \quad (14)$$

The shear stresses at each boundary of the plug are equal to the yield stress of the MR fluid and can be expressed as $\tau_{rx}(r=a) = \tau_y$ and $\tau_{rx}(r=b) = -\tau_y$. Thus,

$$\frac{1}{2} \frac{dP}{dx} a + \frac{C_1}{a} = -\frac{1}{2} \frac{dP}{dx} b - \frac{C_1}{b} \quad (15)$$

or

$$C_1 = -\frac{ab}{2} \frac{dP}{dx} \quad (16)$$

Table 1
List of boundary conditions.

Regions	Boundary conditions
Region I	$R_1 \leq r \leq a$ $u(R_1) = -V_p, \frac{du(a)}{dr} = 0$
Region II	$u(a) = u(b)$ $b \leq r \leq R_2$
Region III	$u(R_2) = -V_p, \frac{du(b)}{dr} = 0$

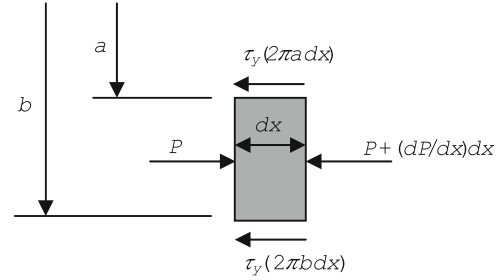


Fig. 4. Free-body diagram of a ring-shaped differential fluid element of thickness $b-a$ and length dx .

Now consider a differential fluid element of thickness $b-a$, length dx as shown in Fig. 4. A force balance on the volume element in the flow direction gives

$$\frac{dP}{dx} \pi (b^2 - a^2) dx + 2\pi \tau_y (b+a) dx = 0 \quad (17)$$

or

$$\frac{dP}{dx} = -\frac{2\tau_y}{b-a} \quad (18)$$

C_1 can be determined by substituting Eq. (18) into Eq. (16) as

$$C_1 = \frac{ab\tau_y}{b-a} \quad (19)$$

The law of conservation of mass requires that the total volume flow rate through the annular gap must be equal to the summation of the volume flow rates through the three regions: Region I, II and III. Once the velocity profiles at each of the three regions are known, the total volume flow rate can be determined from

$$\begin{aligned} Q_T &= 2\pi \int_{R_1}^a \left[-\frac{1}{4\mu} \frac{dP}{dx} (R_1^2 - r^2) + \frac{C_1}{\mu} \ln\left(\frac{r}{R_1}\right) - \frac{\tau_y}{\mu} (r - R_1) - V_p \right] r dr \\ &+ 2\pi \int_a^b \left[-\frac{1}{4\mu} \frac{dP}{dx} (R_2^2 - b^2) + \frac{C_1}{\mu} \ln\left(\frac{b}{R_2}\right) - \frac{\tau_y}{\mu} (R_2 - b) - V_p \right] r dr \\ &+ 2\pi \int_b^{R_2} \left[-\frac{1}{4\mu} \frac{dP}{dx} (R_2^2 - r^2) + \frac{C_1}{\mu} \ln\left(\frac{r}{R_2}\right) - \frac{\tau_y}{\mu} (R_2 - r) - V_p \right] r dr \end{aligned} \quad (20)$$

On the other hand, by definition, the total volume flow rate through the annuli must be equal to the volume flow rate displaced by the piston head, $Q_p = (A_p - A_s) V_p$. Thus, we have

$$Q(a,b) - Q_p = 0 \quad (21)$$

There are two unknowns, a and b , but we have only one equation, Eq. (21), at hand. The second equation comes from the substitution of Eq. (18) into Eq. (14)

$$\frac{4}{R_1^2 - R_2^2 + b^2 - a^2} \left[C_1 \ln\left(\frac{a R_2}{b R_1}\right) + \tau_y (R_1 + R_2 - a - b) \right] + \frac{2\tau_y}{b-a} = 0 \quad (22)$$

The Newton–Raphson method is employed to solve the resulting nonlinear system of these two algebraic equations, Eqs. (21) and (22), to determine a and b . Once a and b have been determined the pressure gradient can be determined from Eq. (18). Hence, the pressure drop due to the field-dependent yield stress can be calculated from

$$\Delta P_\tau = -\frac{dP}{dx} L_{\text{active}} \quad (23)$$

where L_{active} is the active pole length exposed magnetic field. Now, the damping force of the MR damper can be determined from

$$F_{\text{rebound}} = -(\Delta P_\tau (A_p - A_s) + F_f + F_{\text{gas}}) \quad (24)$$

$$F_{\text{compression}} = \Delta P_t A_p + F_f + F_{\text{gas}} \quad (25)$$

Note that the damping force of the MR damper varies according to its motion, whether it is in rebound or compression mode.

3.1. Special case: No magnetic field

So far we have performed calculations for the flow of MR fluid induced by a magnetic field. However, in the regions of inactive magnetic field, the regions particularly adjacent to the winding where $\tau_y=0$, MR fluid exhibits a Newtonian like behavior and thus should be evaluated separately. The shear stress across an annular gap was given by Eq. (5). Integrating Eq. (5) with respect to r gives

$$u(r) = \frac{1}{4\mu} \frac{dP}{dx} r^2 + \frac{C_1}{\mu} \ln r + C_2 \quad (26)$$

C_1 and C_2 can be determined from the boundary conditions: At $r=R_1$ $u=-V_p$ and at $r=R_2$ $u=-V_p$. Once the velocity profile is known, one can calculate the total volume flow rate through the flow channel from

$$Q_T = 2\pi \int_{R_1}^{R_2} u(r)r dr \quad (27)$$

Recall that the total volume flow rate through the annuli must be equal to the volume flow rate displaced by the piston head, $Q_p=(A_p-A_s)V_p$. Therefore,

$$Q_T - Q_p = 0 \quad (28)$$

One can solve Eq. (28) for dP/dx and use it to determine the pressure drop due to the viscous effects only as

$$\Delta P_\mu = -\frac{dP}{dx} L_{\text{inactive}} \quad (29)$$

And thus the damping force

$$F_{\text{rebound}} = -(\Delta P_\mu (A_p - A_s) + F_f + F_{\text{gas}}) \quad (30)$$

$$F_{\text{compression}} = \Delta P_m A_p + F_f + F_{\text{gas}} \quad (31)$$

where $L_{\text{inactive}} = L - L_{\text{active}}$. Note that for the case of zero magnetic field L_{inactive} is equal to L .

4. Experimental study

4.1. Test set-up

The MR damper is subjected to sinusoidal excitations on a mechanical scotch-yoke type damper dynamometer to validate the models. The primary components of the test set-up are shown in Fig. 5. The shock machine has its own software to collect the data from the data card and use them to plot force vs. time, force vs. displacement and force vs. velocity graphs for each test. A programmable "GWinstek PPE 3223" power supply is used to feed current to the MR damper. The machine also has an IR temperature sensor to read the temperature data during the tests. The damper is fixed to the machine via grippers as shown in the Fig. 5. The machine excites the damper's piston rod sinusoidally, while a load cell of 22 kN measures the force on the damper and a linear variable displacement transducer (LVDT) measures the displacement of the piston rod as well as the relative velocity between the two ends of the damper.

4.2. Test procedure and conditions

A series of tests is conducted to determine the dynamic response of the damper by varying the applied current from 0 to 2 A in increments of 0.2 A, while maintaining the frequency at

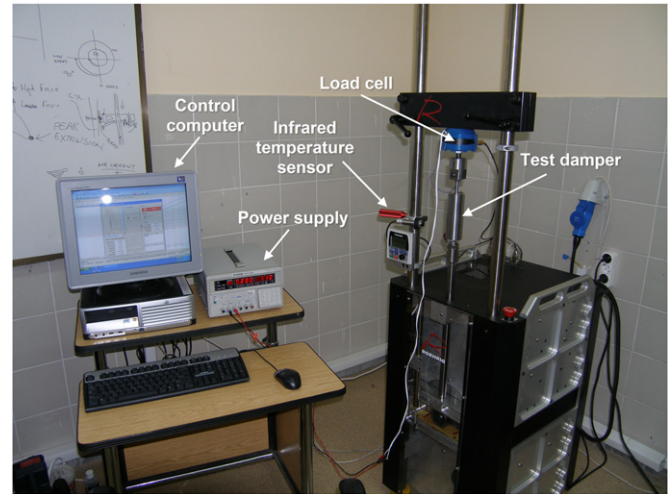


Fig. 5. Photograph of the test set-up.

Table 2

Technical specifications of SAUMRD002.

Parameter	Value	Unit
Damping force, F	200–2000	N
Operating current, I	0–2	A
Yield strength, τ_y	5750–23500	Pa
Plastic viscosity, μ	0.07	Pa s
Piston velocity, V_p	0–0.2	m/s
Piston diameter, D_p	0.039	m
Shaft diameter, D_s	0.010	m
Maximum stroke, S	0.055	m
Inner diameter of the cylinder, $D_{\text{cyl},i}$	0.040	m
Gap of the flow channel, g	0.0004	m
Length of the flow channel, L	0.020	m
Active pole length, L_{active}	0.008	m
Outer diameter of the flow channel, $D_{\text{channel},o}$	0.032	m
Inner diameter of the flow channel, $D_{\text{channel},i}$	0.03102	m
Total length of the damper at its maximum extension	0.27	m

constant levels of 0.63, 1.27, 1.90 and 2.54 Hz, respectively. The technical specifications of the test damper are given in Table 2.

5. Test results and validation of the proposed model

5.1. Test results

Fig. 6 represents the force vs. velocity and force vs. displacement plots for an oscillation frequency of 2.54 at a displacement amplitude of 12.5 mm. Similar test results were observed for other frequencies as well. The gas and friction forces measured to be approximately 60 and 110 N, respectively. As can be seen from Fig. 6, the lowest damping force which is only due to the viscous forces occurs at zero current input, and the damping force increases with increasing current inputs. It is clear from Fig. 6 that the controllable damping forces can easily be acquired by changing the electric current input. This implies that an MR damper can be viewed as a versatile device in the sense that it can provide infinitely variable load cycles within a specified dynamic operating range compared to a classical dashpot.

For an MR damper the increase in the damping force due to applied current is not unlimited. A careful look at Fig. 6 reveals

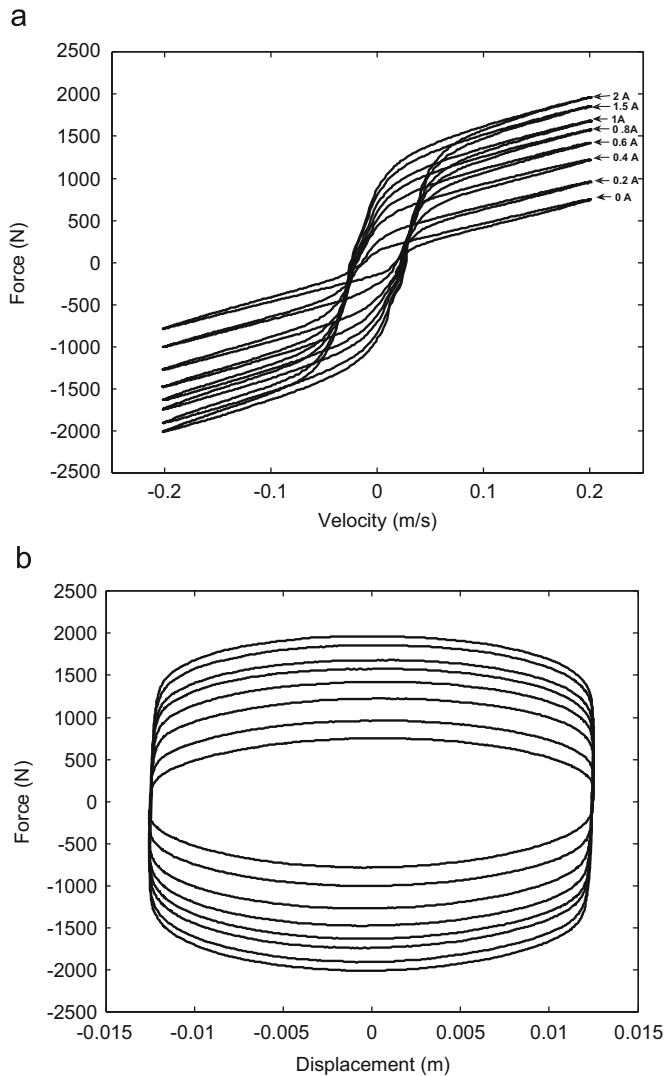


Fig. 6. Force vs. velocity and force vs. displacement plots of SAUMRD002 at 2.54 Hz sinusoidal excitation.

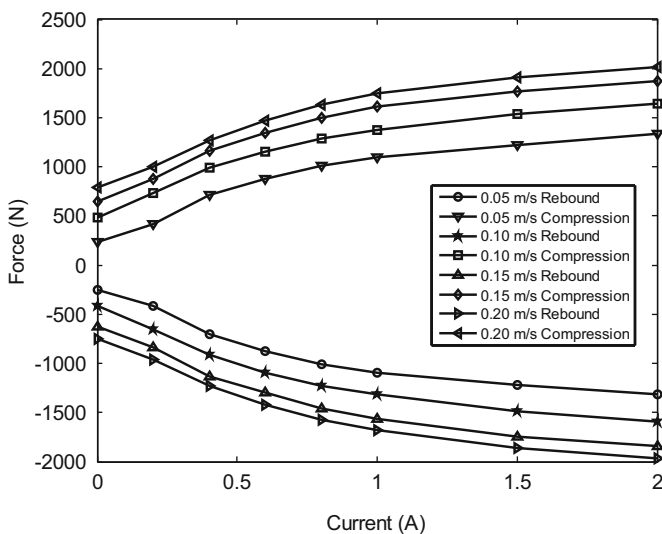


Fig. 7. Force vs. current plots of SAUMRD002.

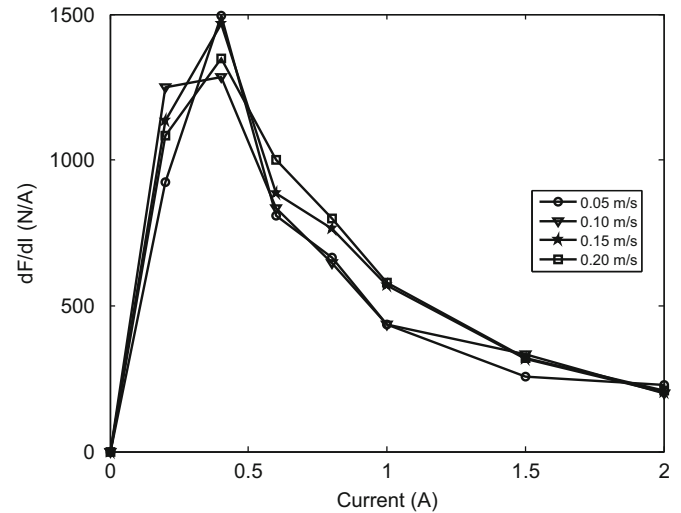


Fig. 8. Susceptibility of SAUMRD002 to the applied current.

that this increase decays gradually as the applied current increases, especially, to its high values, which is illustrated by Figs. 7 and 8 for convenience. One can observe from Fig. 7 that the variation in force levels off in the vicinity of 2 A. In Fig. 8, the plot of the derivative of force with respect to current (dF/dI) versus current is sketched in order to depict the susceptibility of the damping force to the applied current. It is clear from Fig. 8 that the damping force increases with the applied current to reach its peak value around 0.5 A and then decreases asymptotically. This is due to the fact that the MR fluid is magnetically saturated within a certain range of magnetic field. This phenomenon is of critical importance in design considerations of an MR damper and should be taken into account properly for determination of the best efficient operating range of the damper. Also, operating at higher current inputs may cause the temperature of the coil wire to rise, which is not desired.

5.2. Validation of the theoretical flow model

In this section the fluid dynamics model has been verified by comparing the model results with the experimental data. Comparisons between the model and experimental values are presented in Fig. 9. It is observed that the predicted values with the fluid dynamics model agree well with the measured values, except in the hysteretic region seen in the force vs. velocity plot. One can infer from Fig. 9a that as the current input increases, the local slopes of the force vs. velocity curves increase. This can be attributed to the fact that the apparent viscosity of the MR fluid changes with shear-strain rate leading to shear-thinning or -thickening behavior of the MR fluid. The Bingham plastic model used in this study does not account for such behavior assuming the plastic viscosity to be constant. However, the Herschel-Buckley constitutive model with $\tau = \tau_y + K\dot{\gamma}^n$, where τ_y is the yield stress of the MR fluid, $\dot{\gamma}$ is the deformation rate, and K and n are the consistency and flow indexes both of which are determined experimentally, can be used to predict this characteristic of MR fluids [12,15]. Further studies on shear-thinning or -thickening behaviors of MR fluids can be found in the literature, such as [15].

There is also another fluid mechanics model called as Biviscous model to simulate the force response of the MR damper. In this model, the damping behavior is due to leakage, defined as a second path of Newtonian flow in addition to the Bingham plastic flow through an ER/MR valve. Leakage is typically introduced to smooth the force response of the damper as the damper

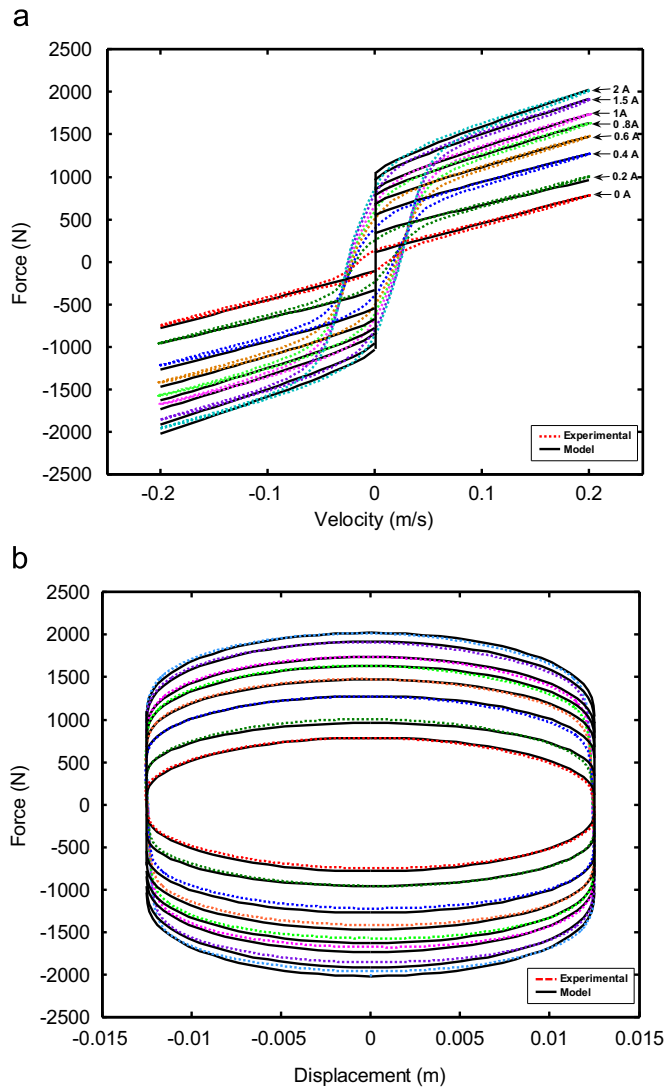


Fig. 9. Comparisons between the model predictions and experimental data: (a) force vs. velocity and (b) force vs. displacement.

undergoes transitions through the low velocities, whereas in the absence of leakage ER/MR dampers usually exhibit a high-frequency chatter in their force response [16]. As can be seen from Fig. 9a, Bingham Plastic model like other fluid mechanics based models such as Herschel–Bulkley and Biviscous cannot describe the hysteretic behavior of MR dampers. Nevertheless Bingham Plastic model can still be successfully adopted to predict the dynamic operating range of MR dampers owing to its simplicity. The total area enclosed in force vs. displacement curves represents the energy dissipated by an MR damper. It is clear from Fig. 9b that higher applied magnetic field will result in higher energy dissipation.

5.3. Modeling the hysteretic behavior of MR damper

The dislocation movement and plastic slipping among molecular chains or crystal lattices consume energy such that the restoring force of an MR damper always delays the input displacement or velocity. This phenomenon of energy dissipation is generally referred to as hysteresis. Different models have been studied in the literature to describe the hysteretic behavior of MR dampers. These models can be classified into two main categories as quasi-static flow models and dynamic models. While

the quasi-static flow models can be successfully adapted to design MR dampers, they unfortunately fail to capture the dynamic operational behavior of these dampers. That is, a quasi-static flow model such as Bingham plastic model can describe the force–displacement range of an MR damper effectively in the preliminary design process; however, it is not capable of describing the highly hysteretic force–velocity characteristic, which is, in fact, of crucial importance for a successful control performance of the damper. Therefore, a dynamic hysteresis model is needed to simulate the hysteresis phenomenon of MR dampers. To this end, various models have been proposed in the literature such as parametric viscoelastic–plastic model based on the Bingham model [9], the Bouc–Wen model [17], non-parametric models [18], and many more. In this study, the model used by Guo and Hu [1] to define an additional nonlinear stiffness is exploited and modified to give more accurate results. The model is given by

$$F(t) = f_0 + C_b \dot{x}(t) + \frac{2}{\pi} f_y \tan^{-1} \left\{ k [\dot{x}(t) - \dot{x}_0 \operatorname{sgn}(\ddot{x}(t))] \right\} \quad (32)$$

where F represents the damping force of the MR damper, f_0 the preload of the nitrogen accumulator, C_b the coefficient of viscous damping, f_y the yielding force, k the shape coefficient, \dot{x}_0 the hysteretic velocity, \dot{x} and \ddot{x} the excitation velocity and acceleration of the piston in the damper, respectively. This mathematical model is developed based on some physical phenomena. While the first term is to represent the preload force of the pressurized nitrogen gas in the accumulator, the second term is to describe the viscous force of the damper and the third one is to reflect the observed hysteretic behavior, respectively. The mathematical descriptions of the first two terms come from classical mechanics, whereas of the third one is developed based on the definition of a trigonometric arctangent function which best resembles the characteristic force–velocity curve of the damper. Further, the two terms in the braces of the arctangent function are to account for the lag in the force response to a sinusoidal excitation.

In the model $x(t) = a \sin(\omega t)$, $\dot{x}(t) = a\omega \cos(\omega t)$, and $\ddot{x}(t) = -a\omega^2 \sin(\omega t)$ where a is the displacement amplitude and ω is the angular velocity. In Eq. (32), f_0 , C_b , f_y , k , and \dot{x}_0 are the unknown parameters and to be determined on the basis of experimental data by using least-square curve fitting method.

It is observed that there is a general good agreement between the estimated and measured values except at lower current inputs, i.e. 0 and 0.2 A of the highest excitation velocity of 0.2 m/s (Fig. 10). We have reasoned that this could be presumably due to the fluid inertial force, which becomes more significant at lower current inputs compared to induced yield stress force, as the excitation acceleration increases. Starting from this point, we modified the model given by Eq. (32) by adding an inertial force term in order to improve the agreement

$$F(t) = f_0 + C_b \dot{x}(t) + \frac{2}{\pi} f_y \tan^{-1} \left\{ k [\dot{x}(t) - \dot{x}_0 \operatorname{sgn}(\ddot{x}(t))] \right\} + m \ddot{x}(t) \quad (33)$$

where m represents the virtual mass which has to be determined based on the experimental data. It is obvious from Fig. 11 that the proposed modified algebraic model (mAlg) removed the disagreement at the mention lower current input region. Model parameter estimates are given in Table 3.

Fig. 12 represents the velocity (0–0.2 m/s) averaged variation of model parameters with the applied current for mAlg model. Each parameter in Eqs. (32) and (33) has an effect on the shape of the curve such that f_0 slides the curve up or down maintaining the shape of the whole curve, f_y controls the dynamic force range, C_b controls the slope of the whole curve, whereas k and \dot{x}_0 controls the slope and the span of the low velocity hysteresis loop, respectively. In addition to these parameters, m controls the span of the high velocity hysteresis loop.

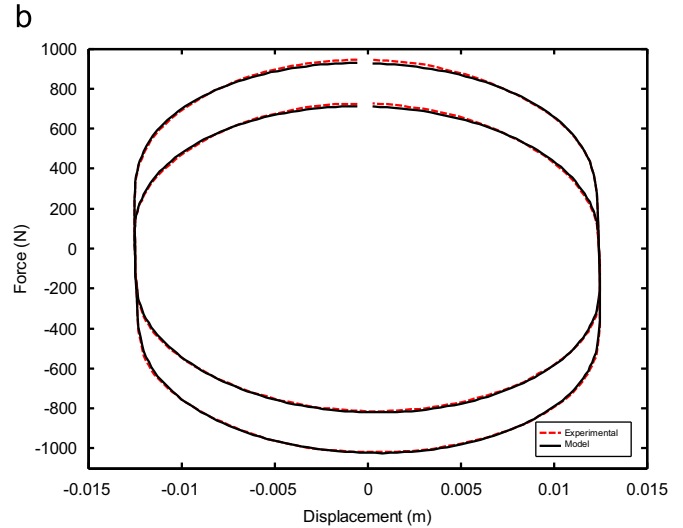
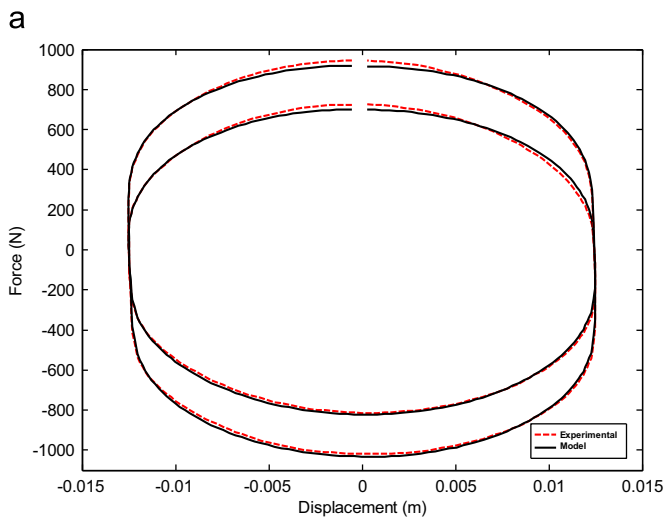
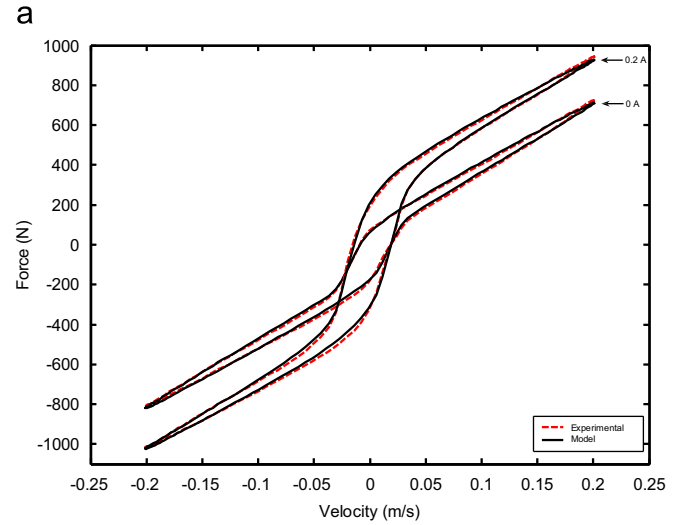
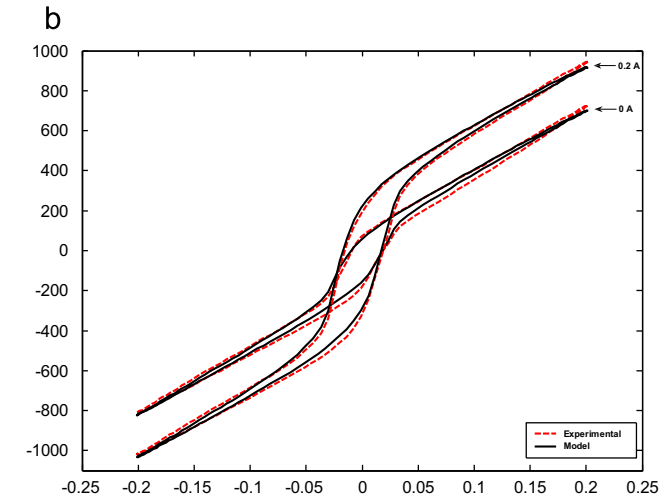


Fig. 10. Hysteretic loops of damping force of SAUMRD002 with respect to (a) velocity and (b) displacement obtained from the model given by Eq. (32) at current inputs of 0 and 0.2 A.

Fig. 11. Hysteretic loops of damping force of SAUMRD002 with respect to (a) velocity and (b) displacement obtained from the model given by Eq. (33) at current inputs of 0 and 0.2 A.

Under these considerations, one can reveal that there is direct correlation between the model parameters and the experimental data by comparing Fig. 12 against Fig. 6a. It should be noted that a small change in the parameters may correspond to relatively large changes in the experimental data. For instance, one can expect f_y to increase with the current input since the dynamic damping force of the MR damper increases with the applied current. A closer look at Fig. 12 will indicate that it really does. The variation in all other parameters can be validated in a similar fashion.

More emphasis should be made on the additional parameter m as it enhanced the success of the model. As discussed previously, m controls the span of the high velocity hysteresis loop. It can be seen from Fig. 6a, the span of the high velocity hysteresis loop decreases with the applied current. Now, a careful look at Fig. 12 will reveal that m decreases with the current input as well, which agrees with our expectation.

Also, it can be deduced from the Fig. 12 that the variation in the model parameters levels off as the applied current approached its maximum value 2 A, as discussed in the previous sections.

In addition to graphical comparison of the mAlg model with the Alg model, we intend to compare these two models with also a previously suggested modified Bouc–Wen’s (mBW) model through an error analysis in order to better reveal the success of the mAlg model. One of the earliest models that have been

extensively used in modeling dynamic behavior of hysteretic systems is the standard Bouc–Wen model, which is extremely versatile and can exhibit a wide variety of hysteretic behavior. However, the nonlinear force–velocity response of the Bouc–Wen model does not roll-off in the region where the acceleration and velocity have opposite signs and the magnitudes of the velocities are small, Spencer et al. [16] proposed a modified version of the Bouc–Wen model in order to predict the dynamic behavior of the MR damper in this region to enhance the success of the model. The modified Bouc–Wen model was given by

$$F = \alpha z + c_0(\dot{x} - \dot{y}) + k_0(x - y) + k_1(x - x_0) \quad (34)$$

where the evolutionary variable z is governed by

$$\dot{z} = -\gamma|\dot{x} - \dot{y}||z||z|^{n-1} - \beta(\dot{x} - \dot{y})|z|^n + A(\dot{x} - \dot{y}) \quad (35)$$

where

$$\dot{y} = \frac{1}{(c_0 + c_1)} \{ \alpha z + c_0 \dot{x} + k_0(x - y) \} \quad (36)$$

In this modified model, the accumulator stiffness is represented by k_1 and the viscous damping observed at larger velocities is represented by c_0 . A dashpot, represented by c_1 , is included in the model to produce the roll-off that was observed in the experimental data at low velocities, k_0 is present to control the

Table 3
Parameter estimates for mAlg model.

V(m/s)	Parameters	Applied current, I (A) (mAlg)								
		0	0.2	0.4	0.6	0.8	1	1.5	2	
0.05	C_b	3427.4	3685.1	4459.2	5520.5	5788.3	6086.3	5900.3	6859.4	
	f_0	-42.1	-36.7	-34	-35.3	-34	-31.9	-28.3	-27.3	
	f_y	8.4	15.5	22.5	25	27.5	28.9	31.5	32.1	
	k	428.4	433.9	334.5	326.3	293.4	288.3	244	266.4	
	m	55.3	48.8	30.6	22.3	1	12.5	-33.4	-75.3	
	\dot{x}_0	0.0019	0.0006	0.0017	0.0021	0.0023	0.0024	0.003	0.0033	
0.1	C_b	3264	3242.8	3470.7	3567.7	3721	3982.2	4325	4384.8	
	f_0	18.3	23.3	22.7	16.2	15.7	12.6	13.6	13.9	
	f_y	11.3	19.5	25.1	28.4	30.6	31.5	33.7	35.1	
	k	243.4	164.3	149.4	133.2	130.8	134.9	128.3	131.5	
	m	7.7	6.9	6	-1.8	-4.3	-5.1	-12.1	-13.3	
	\dot{x}_0	0.0062	0.0053	0.006	0.0072	0.0075	0.0078	0.0087	0.0106	
0.15	C_b	3264	3211.8	3235.8	3284	3391.3	3479.4	3590.6	3627.7	
	f_0	-32.5	-31.5	-33.8	-32.7	-35	-34.8	-37.3	-36.2	
	f_y	11.3	19.6	26.3	29.5	31.9	33.5	35.8	37.2	
	k	243.4	107.5	92.8	83.5	80.8	80.1	83.5	82.7	
	m	7.7	-3.4	-5.7	-7.2	-9.6	-12.7	-14.6	-17.3	
	\dot{x}_0	0.0062	0.0051	0.0069	0.008	0.0094	0.0093	0.0108	0.0114	
0.2	C_b	3175.6	2996.8	2930.4	2872.7	2824.5	2818	2915.7	2847.2	
	f_0	-54.5	-47.7	-48.2	-45.4	-48.9	-50.8	-52.9	-52.2	
	f_y	11.6	19.8	26.2	30.2	33.1	34.6	37	38.7	
	k	108	75.3	67	60.8	55.6	57.2	56.1	53.7	
	m	-0.7	-2	-3.2	-5.6	-8.6	-8.2	-10.7	-12.5	
	\dot{x}_0	0.0078	0.0097	0.0111	0.0127	0.0137	0.0142	0.0154	0.0171	

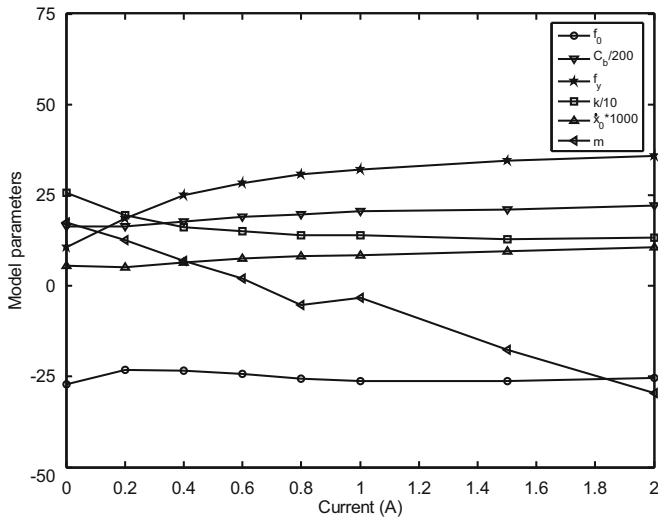


Fig. 12. Velocity (0–0.2 m/s) averaged variation of the model parameters with current input.

stiffness at large velocities and x_0 is the initial displacement of spring k_1 associated with the nominal damper force due to the accumulator. A schematic for the model is given in Fig. 13.

For all of the models, the error between the predicted force and the measured force was calculated as a function of time, displacement and velocity over a complete period. The following expressions were used to represent the errors [17]

$$E_t = \frac{\varepsilon_t}{\sigma_F}, E_x = \frac{\varepsilon_x}{\sigma_F}, E_{\dot{x}} = \frac{\varepsilon_{\dot{x}}}{\sigma_F} \tag{37}$$

where

$$\varepsilon_t^2 = \int_0^T (F_{exp} - F_{pre})^2 dt \tag{38}$$

$$\varepsilon_x^2 = \int_0^T (F_{exp} - F_{pre})^2 \left| \frac{dx}{dt} \right| dt \tag{39}$$

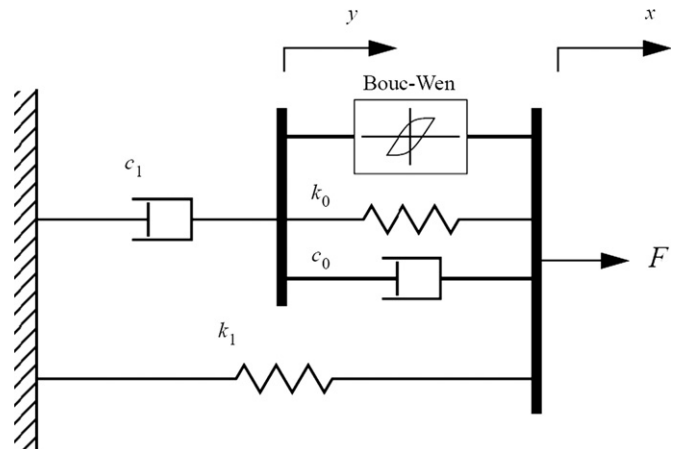


Fig. 13. The modified Bouc-Wen model for the MR damper.

$$\varepsilon_x^2 = \int_0^T (F_{exp} - F_{pre})^2 \left| \frac{dx}{dt} \right| dt \tag{40}$$

$$\sigma_F^2 = \int_0^T (F_{exp} - \mu_F)^2 dt \tag{41}$$

The resulting normalized errors are presented in Table 4.

It is seen that although all the three models are equivalent at the excitation velocities of 0.05, 0.10, and 0.15 m/s, mAlg model is remarkably successful at the highest excitation velocity of 0.2 m/s. This is presumably due to effect of the added inertial term to the Alg model because the inertial forces are dominant as the excitation acceleration is increased. Also if we focus on the highest excitation velocity, when comparing the Alg model and mAlg model, one can note that as the current inputs increases the error differences between the Alg model and the mAlg model decreases. This can be attributed to the fact that the viscous forces and thus inertial force effects are getting less dominant with the

Table 4
Error norms for each model.

V (m/s)	0.05			0.10			0.15			0.20		
	E_t	E_x	$E_{\dot{x}}$									
Model												
mBW												
0.0	0.019	0.003	0.007	0.018	0.004	0.014	0.018	0.005	0.020	0.021	0.007	0.029
0.2	0.041	0.004	0.018	0.025	0.004	0.021	0.018	0.004	0.022	0.020	0.006	0.031
0.4	0.044	0.005	0.019	0.023	0.004	0.019	0.021	0.004	0.025	0.023	0.006	0.038
0.6	0.049	0.005	0.021	0.022	0.003	0.019	0.022	0.005	0.026	0.026	0.007	0.041
0.8	0.028	0.003	0.013	0.023	0.004	0.020	0.021	0.005	0.027	0.026	0.007	0.042
1.0	0.030	0.003	0.013	0.022	0.003	0.019	0.022	0.005	0.027	0.026	0.007	0.042
1.5	0.030	0.003	0.013	0.021	0.003	0.018	0.021	0.004	0.027	0.025	0.006	0.042
2.0	0.028	0.003	0.012	0.021	0.004	0.018	0.022	0.004	0.027	0.026	0.007	0.043
Average	0.034	0.004	0.015	0.022	0.004	0.019	0.021	0.005	0.025	0.024	0.007	0.038
Alg												
0.0	0.056	0.007	0.023	0.031	0.006	0.025	0.024	0.006	0.029	0.028	0.009	0.042
0.2	0.035	0.005	0.015	0.020	0.004	0.016	0.016	0.004	0.018	0.021	0.007	0.032
0.4	0.029	0.004	0.012	0.019	0.003	0.017	0.018	0.004	0.022	0.022	0.006	0.034
0.6	0.029	0.004	0.013	0.022	0.003	0.019	0.020	0.004	0.025	0.024	0.006	0.039
0.8	0.029	0.003	0.013	0.023	0.003	0.020	0.020	0.004	0.025	0.025	0.007	0.040
1.0	0.030	0.003	0.014	0.024	0.003	0.021	0.022	0.004	0.028	0.026	0.007	0.042
1.5	0.031	0.003	0.014	0.024	0.003	0.021	0.023	0.004	0.030	0.027	0.007	0.044
2.0	0.031	0.003	0.014	0.023	0.004	0.021	0.024	0.005	0.032	0.027	0.007	0.046
Average	0.034	0.004	0.015	0.023	0.004	0.020	0.021	0.005	0.026	0.025	0.007	0.040
mAlg (This study)												
0.0	0.035	0.004	0.014	0.018	0.003	0.023	0.017	0.004	0.019	0.015	0.005	0.022
0.2	0.034	0.004	0.025	0.022	0.003	0.024	0.020	0.003	0.022	0.013	0.004	0.025
0.4	0.035	0.004	0.020	0.020	0.003	0.026	0.021	0.003	0.020	0.014	0.004	0.022
0.6	0.035	0.004	0.021	0.022	0.004	0.024	0.020	0.004	0.024	0.015	0.004	0.024
0.8	0.035	0.004	0.020	0.023	0.004	0.026	0.022	0.004	0.026	0.015	0.004	0.024
1.0	0.033	0.004	0.021	0.023	0.004	0.027	0.019	0.004	0.021	0.017	0.004	0.025
1.5	0.034	0.004	0.019	0.021	0.004	0.026	0.022	0.004	0.025	0.017	0.004	0.026
2.0	0.035	0.004	0.019	0.023	0.004	0.028	0.023	0.004	0.025	0.017	0.004	0.025
Average	0.035	0.004	0.020	0.022	0.003	0.026	0.021	0.004	0.023	0.016	0.004	0.024

increased current inputs. This actually agrees with our intuitions since we added an inertial term to modify the model to account for the inertial effects of the MR fluid.

Apart from its high accuracy, mAlg model is also more preferable in terms of its low computational expenses compared to differential modified Bouc–Wen's model which is highly computationally demanding. It is hoped that the present improved model will aid to develop more effective control strategies and algorithms for MR dampers.

6. Conclusions

An experimental and a theoretical analysis were conducted to model the dynamic behavior of an MR damper. To this end, an MR damper was designed, manufactured and tested on a conventional shock machine. A flow analysis of an MR damper was done based on the Bingham plastic constitutive model and the prediction results was compared against the test data. The comparisons showed that there was a very good agreement between the flow model and test results. Therefore, it was concluded that the Bingham plastic model could satisfactorily predict the operational force range of the MR damper. However, this model was found to be not capable of capturing the inherent hysteretic behavior of the MR damper, which is of crucial importance for a successful control performance. For this reason, an algebraic model (Alg), which we have modified by adding an inertial force term (mAlg), was employed to describe the hysteretic behavior of the MR damper. The unmodified and modified forms of the algebraic model, which are parametric in nature, were compared with the experimental data. It was shown that the mAlg model reduced the errors associated with force vs. time, force vs. velocity and force vs.

displacement characteristics remarkably. Then, in order to better reveal the success of the mAlg model, Alg model, mAlg model, and a previously suggested modified Bouc–Wen's (mBW) model were compared through a quantitative error analysis. It was seen that although all three models are equivalent at the excitation velocities of 0.05, 0.10, and 0.15 m/s, mAlg model is remarkably successful at the highest excitation velocity of 0.2 m/s. This is presumably due to effect of the added inertial term to the Alg model because the inertial forces are dominant as the excitation acceleration is increased. And, when comparing Alg and mAlg models, the reductions in errors were found to be over 50% especially for low currents rated at the highest excitation velocity of 0.2 m/s. This is presumably attributed to the fact that the inertial forces become more comparable to the induced yield force at lower current inputs as the excitation acceleration is increased. The effect of the inertial force vanishes at high current inputs since the induced yield forces are dominated with the increase in the current input, as expected.

It was deduced that the proposed mAlg model could overcome the shortcomings of the original Alg model and it can successfully be employed to describe the hysteretic behavior of the MR damper so as to develop effective control algorithms due to its high accuracy, low computational expenses compared to a traditionally widely adopted modified Bouc–Wen's model, which is computationally highly demanding.

Acknowledgements

The authors gratefully acknowledge to The Scientific and Technological Research Council of Turkey (TÜBİTAK) for making this project possible under Grant No. 104M157. The authors also

acknowledge to TÜBİTAK-Münir Bırsel Graduate Scholarship Foundation for its financial support to the first author (Şevki Çesmecı).

References

- [1] Guo D, Hu H. Nonlinear-Stiffness of a magnetorheological fluid damper. *Nonlinear Dynamics* 2005;40:241–9.
- [2] Chooi WW, Oyadiji SO. Design, modeling and testing of a magnetorheological (MR) dampers using analytical flow solutions. *Computers & Structures* 2008;86:473–82.
- [3] Choi S.B., Lee H.S., Hong S.R., and Cheong C.C. Control and response characteristics of a magnetorheological fluid damper for passenger vehicles. *Smart Structures and Integrated Systems*. In: *Proceedings of SPIE conference on smart materials and structures* Edited by Norman M. Wereley 2000; 3895:pp. 438–443.
- [4] Kamath GM, Wereley NM, Jolly MR. Characterization of magnetorheological helicopter lag dampers. *Journal of the American Helicopter Society* 1999;44(3):234–48.
- [5] Gordaninejad F, Kelso SP. Fail-Safe magneto-rheological fluid dampers for off-highway. *High-Payload Vehicles*. *Journal of Intelligent Material Systems and Structures* 2001;11(5):395–406.
- [6] Lee T.Y., Kawashima K. Semi-active control of seismic-excited nonlinear isolated bridges. In: *Proceedings of the eighth US national conference on earthquake engineering*. April 18–22, San Francisco, California, USA 2006:pp. 423.
- [7] Unsal M. Semi-active vibration control of a parallel platform mechanism using magnetorheological damping. Ph. D. Dissertation: University of Florida; 2006.
- [8] Kamath GM, Hurt MK, Wereley NM. Analysis and testing of Bingham plastic behavior in semi-active electrorheological fluid dampers. *Smart Materials and Structures* 1996;5:576–90.
- [9] Wereley NM, Lindler J, Rosenfeld N, Choi YT. Biviscous damping behavior in electrorheological shock absorbers. *Smart Materials and Structures* 2004;13: 743–52.
- [10] Wang XJ, Gordaninejad F. Flow analysis and modeling of field-controllable, electro- and magneto-rheological fluid dampers. *Journal of Applied Mechanics—Transactions of the ASME* 2007;74(1):13–22.
- [11] Jolly M.R., Bender J.W., and Carlson J.D. Properties and applications of commercial magnetorheological fluids. In: *Proceedings of the SPIE fifth annual international symposium on smart structures and materials*: San Diego, CA 1998.
- [12] Wang XJ, Gordaninejad F. Flow analysis of field-controlled electro- and magneto-rheological fluids using Herschel–Bulkley model. *Journal of Intelligent Material Systems and Structures* 1999;10(8):601–8.
- [13] Gavin HP, Hanson RD, Filisko FE. Electrorheological dampers. Part 1: Analysis and Design. *Journal of Applied Mechanics, ASME* 1996;63(9): 669–75.
- [14] Yang G, Spencer Jr. BF, Carlson JD, Sain MK. Large-scale MR fluid Dampers: modeling, and dynamic performance considerations. *Engineering Structures* 2002;24(3):309–23.
- [15] Dimock G.A., Lindler J.E., and Wereley N.M. Bingham Biplastic analysis of shear thinning and thickening in magnetorheological dampers, In: *Proceedings of the SPIE's seventh international symposium on smart structures and materials*, Newport Beach, CA, 2000, pp. no:398549.
- [16] Wereley NM, Lindler J, Rosenfeld N, Choi Y-T. Biviscous damping behavior in electrorheological shock absorbers. *Smart Material and Structures* 2004;13: 743–52.
- [17] Spencer Jr. BF, Dyke SJ, Sain MK, Carlson JD. Phenomenological model of a magnetorheological damper. *Journal of Engineering Mechanics, ASCE* 1997;123:230–8.
- [18] Song X, Ahmadian M, Southward SC. Modeling magneto-rheological dampers with multiple hysteresis nonlinearities. *Journal of Intelligent Material Systems and Structures* 2005;16(5):421–32.